

An Iminostilbene Functionalized Benzimidazoline for Enhanced n-Type Solution Doping of Semiconducting Polymers for Organic Thermoelectrics

Pietro Rossi, Francesca Pallini, Giulia Coco, Sara Mattiello, Wen Liang Tan, Lorenzo Mezzomo, Marco Cassinelli, Guglielmo Lanzani, Christopher R. McNeill, Luca Beverina,* and Mario Caironi*


Doped organic semiconductors play a central role in the development of several innovative optoelectronic and energy harvesting applications. Currently, the realization of thermoelectric generators, which require both hole- and electron-transporting materials with high electrical conductivity, is strongly hindered by the scarce availability of stable solution-processable n-dopants and their limited efficiency. Herein, the synthesis of 4-(1,3-dimethyl-2,3-dihydro-1H-benzimidazol-2-yl)-dibenzazepine (IStBI), a novel derivative belonging to the well-known family of the benzimidazoline compounds, is presented. The functionalization with the planarized and rigid iminostilbene substituent allows, without significantly affecting the compound electronic structure, an efficient intercalation of the dopant molecules inside the ordered regions of thin films of the benchmark n-type polymer poly(*N,N'*-bis-2-octyldodecyl naphthalene-1,4,5,8-bis-dicarboximide-2,6-diyl-alt-5,5'-2,2'-bithiophene) P(NDI2OD-T2). Consequently, a maximum electrical conductivity of $(1.14 \pm 0.13) \times 10^{-2} \text{ S cm}^{-1}$ is recorded, exceeding by one order of magnitude what previously achieved upon solution doping of the reference P(NDI2OD-T2) with benzimidazoline derivatives. The thermoelectric power factor is also simultaneously increased. The findings confirm that tailoring of the dopant chemical structure to improve structural interactions with the host semiconductors can be employed as a successful strategy to achieve more effective n-doping, helping to close the performance gap with p-type materials.

1. Introduction

Doping of organic conjugated materials occurs by blending the semiconductor with reducing (n-doping) or oxidizing (p-doping) compounds with the aim of increasing the charge carrier density and therefore the electrical conductivity σ .^[1] This strategy has been successfully exploited to enable a variety of optoelectronic devices, providing new applications and a low-cost and more sustainable alternative to the standard inorganic technology.^[2–5] For instance, realizing layers with an high σ is of foremost importance in developing organic thermoelectric generators (OTEGs), energy harvesting systems which exploit the Seebeck effect to convert thermal gradients into electrical power.^[6] These devices are foreseen to play a central role in the field of the Internet of Things (IoT) as ideal supply systems for low-power, distributed electronics with room temperature applications, substituting or extending the lifetime of standard batteries.^[7] The thermoelectric properties of a material are defined by the figure of merit $zT = (\sigma S^2 / \kappa) T$, where S is

P. Rossi, G. Coco, M. Cassinelli, G. Lanzani, M. Caironi
Center for Nano Science and Technology@PoliMi
Istituto Italiano di Tecnologia
via Giovanni Pascoli 70, Milan 20134, Italy
E-mail: mario.caironi@iit.it

P. Rossi, G. Coco, G. Lanzani
Physics Department
Politecnico di Milano
Piazza Leonardo da Vinci 32, Milan 20133, Italy
F. Pallini, S. Mattiello, L. Mezzomo, L. Beverina
Department of Materials Science
Università di Milano-Bicocca
via Cozzi 55, Milan 20125, Italy
E-mail: luca.beverina@unimib.it
W. L. Tan, C. R. McNeill
Department of Materials Science and Engineering
Monash University
Clayton VIC 3800, Australia

 The ORCID identification number(s) for the author(s) of this article can be found under <https://doi.org/10.1002/admi.202202416>.

© 2023 The Authors. Advanced Materials Interfaces published by Wiley-VCH GmbH. This is an open access article under the terms of the Creative Commons Attribution License, which permits use, distribution and reproduction in any medium, provided the original work is properly cited.

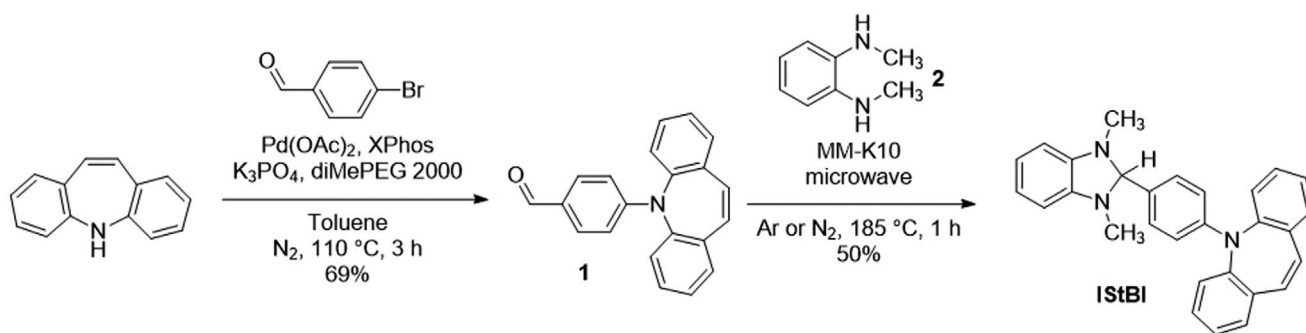
DOI: 10.1002/admi.202202416

the Seebeck coefficient, κ is the thermal conductivity, and T is the average temperature. Due to their disordered structure suppressing phononic transport, organic materials have the advantage of intrinsically possessing a low $\kappa < 1 \text{ W m}^{-1} \text{ K}^{-1}$. Therefore, their characterization is often limited to the evaluation of the power factor, $PF = \sigma S^2$.^[8]

Considering the constraints imposed by device design and fabrication, having both p- and n-type materials with matching transport properties is of pivotal interest to maximize the power generated from a thermoelectric device.^[9] With commercially available p-type materials, such as doped poly(3,4-ethylenedioxythiophene), achieving $\sigma > 1000 \text{ S cm}^{-1}$, the main bottleneck toward the realization of efficient OTEGs is constituted by the lack of solution processable and stable n-type semiconductors with suitable charge transport properties.^[10,11] The lowest unoccupied molecular orbital (LUMO) of most n-type materials sits often above -4.0 eV ; considering a direct electron transfer mechanism, the highest occupied molecular orbital (HOMO) of the dopant is forced to be at higher energies (lower ionization potentials) in order to have charge injection and doping.^[12] These high energy levels make both the dopant molecules and the doped n-type semiconductor prone to reactions with environmental oxygen and water. First n-doping attempts have been performed exclusively in inert conditions using inorganic salts, organometallic compounds and amine-containing molecules, such as tetrakis(dimethylamino)ethylene.^[13–15] These approaches require vacuum processing, a powerful technique in itself but requiring an additional step in solution-based processing scheme of conjugated polymers, and often resulted in poor thermal stability of the doped samples due to out-diffusion phenomena.^[16] A strategy devised to overcome these issues consists in adopting precursor-type dopants, which are chemical compounds that, after incorporation into the semiconductor, need to be activated by temperature or light-exposure to generate the reducing species and effectively dope the host material.^[17] Benzimidazoline derivatives, with 4-(1,3-dimethyl-2,3-dihydro-1H-benzimidazol-2-yl)-N,N-dimethylaniline (N-DMBI) being the first to be employed, are the most common choice among these compounds due to their good solubility in frequently used processing solvents and compatibility with both small molecules and polymer semiconductor.^[18–20] N-DMBI is characterized by an HOMO around -4.4 eV , which makes direct electron transfer not possible in most of the cases. Originally claimed to be air stable, its environmental stability has recently been reconsidered.^[21,22] Despite

the exact reaction mechanism depending on the host material, catalyzing N-DMBI reaction in presence of metallic nanoparticles has been lately demonstrated to yield record conductivity values for a series of organic semiconductors.^[23] Nevertheless, one of the main factors hindering N-DMBI doping efficiency has been associated with its scarce solubility into the semiconductor microstructure.^[24–26] In particular, Schlitz et al. reported that, upon blending with the widely used copolymer poly(*N,N'*-bis-2-octyldodecyl)naphthalene-1,4,5,8-bis-dicarboximide-2,6-diyl-alt-5,5'-2,2'-bithiophene) (P(NDI2OD-T2)), the strong surface segregation of N-DMBI (and also of the diphenylamine-substituted derivative N-DPBI) was limiting the achievable σ value to $5 \times 10^{-4} \text{ S cm}^{-1}$.^[20] Currently the research community is striving to synthesize n-type semiconductors reaching much higher σ and better overall thermoelectric properties, with the notable example of the very recently reported self-doped poly(benzodifurandione) showing $\sigma > 2000 \text{ S cm}^{-1}$.^[27–31] In parallel, studies dedicated to the tuning of the benzimidazoline derivative, realizing alternative chemical structures have also emerged aiming at improving the host-dopant miscibility and reaction efficiency.^[26,32–34] Introducing longer linear and branched dialkyl-substituents on the benzimidazoline core was shown to increase the affinity of the dopant with the apolar side chains of P(NDI2OD-T2) leading to improved σ values. In a similar way adding glycol groups helped miscibility with the polar fullerene derivatives.^[32,34]

In this context, we synthesized a novel benzimidazoline derivative 4-(1,3-dimethyl-2,3-dihydro-1H-benzimidazol-2-yl)-dibenzazepine, referred to as IStBI (Scheme 1), and tested its doping efficacy in solid-state blends with P(NDI2OD-T2), which is up to this date still one of the few commercially available n-type polymers. Despite strong charge localization phenomena limiting its maximum conductivity, this material still constitutes a benchmark for doping studies.^[35] Evidence, collected through the analysis of the changes in the microstructure and topography as a function of IStBI concentration, suggest that the chemical functionalization leads to a more effective intercalation of the dopant inside the polymeric host crystalline regions. Therefore, the introduction of a substituent characterized by a higher rigidity, planarity and electronic conjugation compared to the dialkyl groups of N-DMBI improves the dopant solid-state solubility in P(NDI2OD-T2) thin films. These enhanced dopant-semiconductor structural interactions account for the improved electrical conductivity value, reaching $\sigma \approx 10^{-2} \text{ S cm}^{-1}$, which is the highest reported value for benzimidazoline doping of P(NDI2OD-T2).



Scheme 1. Reaction scheme for 4-(1,3-dimethyl-2,3-dihydro-1H-benzimidazol-2-yl)-dibenzazepine (IStBI).

2. Results

2.1. Chemical Synthesis

Scheme 1 shows the synthetic pathway leading to 4-(1,3-dimethyl-2,3-dihydro-1H-benzimidazol-2-yl)-dibenzazepine (IStBI). The key step of the protocol is a microwave-assisted acid catalyzed condensation reaction in heterogeneous phase between 4-(5H-dibenzo[b,f]azepin-5-yl)benzaldehyde (1) and *N,N'*-dimethyl-1,2-phenylenediamine (2). This procedure was inspired by the protocol devised by Bonacci et al. to prepare a benzimidazoline derivative.^[36] The starting diamine (2) was obtained following a procedure previously reported by our group, while the aldehyde (1) was synthesized adapting a palladium catalyzed Buchwald-Hartwig amination reaction.^[22,37] The condensation reaction was performed under inert atmosphere using Montmorillonite clay (MM-K10) as heterogeneous acid catalyst, and the product was isolated by dry-flash chromatography performed in the dark. Further details on the synthetic procedures adopted to obtain the molecules used in this work, along with reaction schemes, chemical structures, and NMR analysis, are provided in a dedicated section of the Supporting Information.

2.2. Thermal Characterization of IStBI Derivative

The thermal stability of IStBI was investigated by means of thermogravimetric analysis (TGA): the onset for the temperature-activated degradation process is found to be at ≈ 230 °C (data in Figure S1, Supporting Information). Instead, a melting point T_m of ≈ 180 °C was determined from the endothermic peak in the first heating scan of the differential scanning calorimetry (DSC) thermograms (Figure S2, Supporting Information). In the second heating cycle the exothermic feature present in the 130–180 °C range can be attributed to cold recrystallization of the sample, followed by fusion. Comparing this T_m value to those reported in literature for the reference benzimidazoline derivatives N-DMBI and N-DPBI (Table S1, Supporting Information), it can be observed that IStBI is characterized by the highest T_m . Since the molecular weight of IStBI and N-DPBI are very similar, the sizably higher melting point can be correlated to stronger intermolecular interactions, favored by the planarity of the iminostilbene residue.

2.3. Electrochemical Characterization of IStBI Derivative

Electrochemical characterization was performed to evaluate the effects of the iminostilbene functionalization on the electronic structure of the dopant, directly affecting its redox activity.

Cyclic voltammetry (CV) and differential pulse voltammetry (DPV) of IStBI in acetonitrile solution were performed (data reported in Figure S3, Supporting Information; complete experimental procedure and estimation of the electrochemical frontier orbitals in Supporting Information). DPV measurements were performed to support the CV data due to the poor reversibility of the oxidative process, which is evidenced by the asymmetry of the anodic CV scans. N-DMBI and N-DPBI were also analyzed

Table 1. HOMO and SOMO energies calculated from the CV and DPV measured redox potentials of the benzimidazolines and corresponding triflate salts. Details are included in the Supporting Information.

	HOMO [eV]		SOMO ^{a)} [eV]	
	CV	DPV	CV	DPV
IStBI	−4.61	−4.59	−2.63	−2.60
N-DMBI	−4.61	−4.58	−2.54	−2.52
N-DPBI	−4.60	−4.59	−2.81	−2.80

^{a)}SOMO obtained from the relative radical species.

for direct comparison. As reported in Table 1 the results obtained with both techniques are in good agreement. In particular, IStBI is characterized by an HOMO energy level corresponding to −4.61 eV, which is almost identical to the one measured and also reported in literature for N-DMBI and N-DPBI.^[33] The introduction of a moiety characterized by extended π -conjugation, therefore, does not influence the HOMO level, which remains strongly localized on the benzimidazole ring.^[38,39] Hence, also in the case of IStBI a direct electron transfer process to the host semiconductor has to be ruled-out, being the LUMO level of P(NDI2OD-T2) located around −4.0 eV.^[40] The doping reaction with benzimidazoline derivatives has been proposed to proceed through a thermally activated C–H bond homolytic cleavage leading to the formation of a benzimidazoline radical, with electron transfer to the polymer occurring from the single occupied molecular orbital (SOMO) of this charged species.^[21,25] The energy of the radical SOMO, reported in Table 1 for each species, was estimated from the first reduction potential of the cationic species (IStBI⁺, N-DMBI⁺, and N-DPBI⁺) obtained in acetonitrile solution from the corresponding dissociated triflate salt (IStBI-OTf, N-DMBI-OTf, and N-DPBI-OTf; corresponding voltammograms in Figure S4, Supporting Information). Experimentally we obtained a SOMO of −2.54 eV for N-DMBI in acetonitrile solution, which is coherent with the −2.70 eV value computed by Bardagot et al. through bond dissociation energy calculations starting from the crystalline structure obtained by X-ray diffraction.^[21] The value determined for IStBI is −2.63 eV and it is between those obtained for N-DMBI and N-DPBI. This limited difference, therefore, is not expected to significantly affect the energetics of the doping process, and in any case a downward shift of the SOMO with respect to N-DMBI level is reducing the driving force of the electron transfer process. These experimental results do not however consider how the dopant energy levels are modified when the local chemical environment is represented by polymeric chains, instead of solvent molecules. In future, molecular dynamics simulations will be indeed very useful to gain more insights in the dopant–polymer molecular interactions.^[1,34]

2.4. Structural Characterization of P(NDI2OD-T2)/IStBI Thin Films

The impact of blending different amounts of IStBI molecules on the solid-state microstructure of toluene-cast P(NDI2OD-T2) thin films was evaluated employing grazing incidence wide angle X-ray scattering (GIWAXS). Samples were prepared by mixing in solution the semiconductor and the

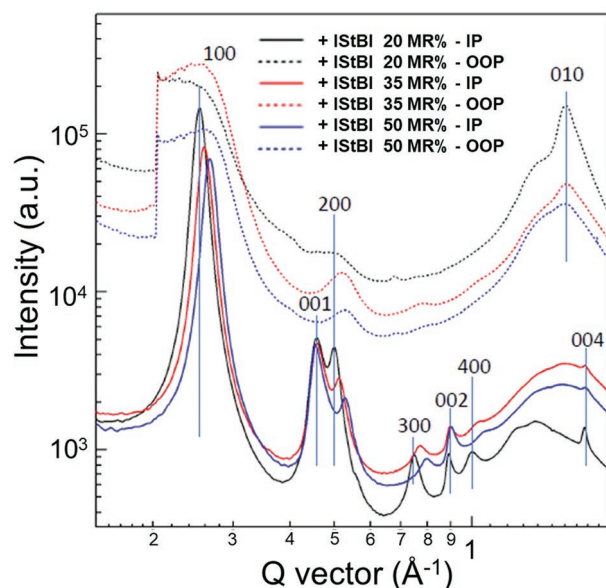


Figure 1. Sector-averaged 1D-GIWAXS patterns along the in-plane (IP, solid line) and the out-of-plane (OOP, dashed line) direction for P(NDI2OD-T2) thin films at different IStBI concentrations. The vertical blue lines are a guide for the eye. The corresponding 2D-GIWAXS diffractograms are reported in Figure S5 in the Supporting Information.

dopant, depositing it on glass substrates via spin-coating, followed by a final thermal annealing step (detailed description in the Experimental Section). Figure S5 in the Supporting Information displays the complete 2D diffraction patterns acquired for samples containing a concentration, expressed as molar ratio (MR%), of 20, 35, and 50 MR% of IStBI. The 1D sector averaged diffractograms, shown in **Figure 1**, are realized by performing linecuts along the in-plane (IP) and out-of-plane (OOP) directions. Independently on the dopant concentration, we can evidence the presence of diffraction features which, according to the literature, can be associated to crystalline polymer domains arranged both in a face-on and an edge-on conformation with respect to the substrate. In detail, a majority face-on component is related to the marked IP (h00) and IP (00l) replicas and to the OOP (010) peak, which are assigned respectively to the lamellar, backbone, and π - π stacking. The OOP (h00) features are instead associated with the lamellar stacking of edge-on oriented regions.^[41,42] Kim and co-workers already observed that the coexistence of both orientations, which in their study-case was promoted by blending P(NDI2OD-T2) with planar and conjugated molecules (tetrathiafulvalene and tetracyanoquinodimethane), improved the bulk interconnectivity and charge transport properties.^[43] An increase in the amount of dopant causes a progressive shift of the (h00) toward higher q -vector values, which in the real space is linked to a reduction of the lamellar repeat unit length. We interpret this finding as evidence of IStBI molecules intercalation between the alkyl side chains of the polymer. This effect was not observed in several works in which N-DMBI and N-DPBI were used.^[20,44] Interestingly other studies, which already report benzimidazole derivative intercalation in the P(NDI2OD-T2) structure, found only the IP (h00) replicas to be affected.^[32,33] We speculate that

IStBI has a higher tendency to solubilize in the host semiconductor matrix. In this light, also the reduction of the OOP (010) diffraction peak can be rationalized as IStBI molecules penetrating the crystalline regions and disrupting the polymer interchain π - π interactions. In general, the decrease in the intensity of the face-on lamellar features can also be attributed to an enhancement of the microstructural disorder. As extensively reported in literature, in semicrystalline copolymers, such as P(NDI2OD-T2), long-range crystalline order is not strictly required to efficiently support charge transport, which is governed by the local interconnectivity between aggregates, therefore maintaining short-range order is sufficient to ensure efficient electrical percolative pathways.^[45,46] The fact that the backbone (00l) replicas are not affected by dopant intercalation indicates that order is preserved on the local scale. Although GIWAXS characterization cannot address disordered phases, the absence of diffraction features that can be connected to IStBI crystalline phase, such as those observed with glycolated naphthalenediimide-based polymers reported in the study of Kiefer et al.,^[47] also points in the direction of improved dopant intercalation and miscibility in the P(NDI2OD-T2).

As shown in Figure S6 in the Supporting Information, increasing the postdeposition annealing temperature while maintaining a fixed IStBI 35 MR% concentration appears to have only a marginal effect, without any substantial change in the diffraction patterns regarding peak positions and widths both in the IP and OOP directions.

Further information on P(NDI2OD-T2) morphology can be collected by acquiring atomic force microscopy images (AFM) of the thin film surface. **Figure 2** presents a comparison between the topography of the pristine polymer film and of a sample containing 35 MR% of IStBI. Both samples display the typical surface appearance of toluene-cast P(NDI2OD-T2) films, showing the presence of elongated fibrillar structures.^[48] Therefore, the supramolecular arrangement of P(NDI2OD-T2), critical for charge transport properties, is preserved. This finding suggests that, although dopant incorporation partially disrupts the crystalline long-range order, as previously shown in the GIWAXS analysis, short-range interconnectivity is preserved. In contrast to several published works, we do not evidence the presence, even when increasing the IStBI concentration to 50 MR% (Figure S7, Supporting Information), of any topographic feature that can be attributed to dopant phase segregation at the thin film surface.^[20,32,49] For all the investigated samples, which are characterized by a thickness of around 65 ± 5 nm, the root-mean-square roughness values extracted from the AFM images are similar and range between 1.5 and 2 nm (details in the Supporting Information), consistent with the absence of dopant phases on the surface. This behavior was directly compared with the limited miscibility of the N-DMBI and N-DPBI derivatives in the semiconductor matrix. To further clarify on the blend homogeneity and on the absence of phase segregated dopant disordered domains, transmission electron microscopy combined with energy-dispersive X-ray spectroscopy mapping could be applied to investigate compositional variations inside the film.^[50,51] This enhancement of the structural affinity between dopant and polymer is expected to influence the efficiency of the doping reaction.

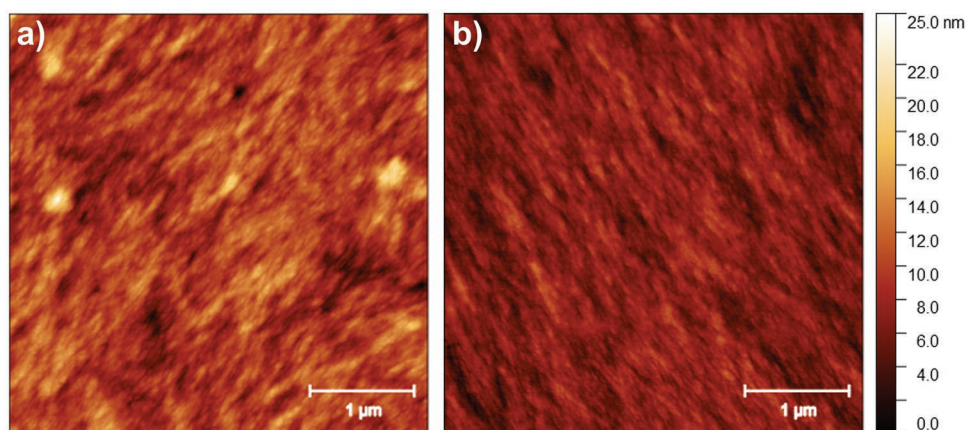


Figure 2. Topography images, collected with AFM operating in tapping mode, of P(NDI2OD-T2) thin films: a) pristine and b) doped with 35% MR of IStBI. All the samples were annealed at 180 °C for 2 h.

2.5. Optical Characterization

A first confirmation of the effective doping interaction between IStBI and P(NDI2OD-T2) comes from the absorption spectra of the toluene-cast polymer thin films, acquired by UV-vis-NIR spectroscopy as a function of increasing dopant concentration in the 0–50 MR% range (**Figure 3**). The spectrum of pristine P(NDI2OD-T2) is characterized by a high energy absorption band at 400 nm, assigned to the π - π^* transition, and a broader feature centered around 705 nm, which is associated to the intrachain charge transfer (ICT) between the donor and acceptor units in the polymer chain and its aggregation state.^[52] Upon addition of IStBI, a progressive bleaching of the neutral polymer ICT band occurs, accompanied by the formation of a band peaking at around 500 nm and an absorption tail above 800 nm. These two features are assigned to polaron states (i.e., radical P(NDI2OD-T2) anions) in agreement with the evidences from spectroelectrochemistry and charge modulation spectro-

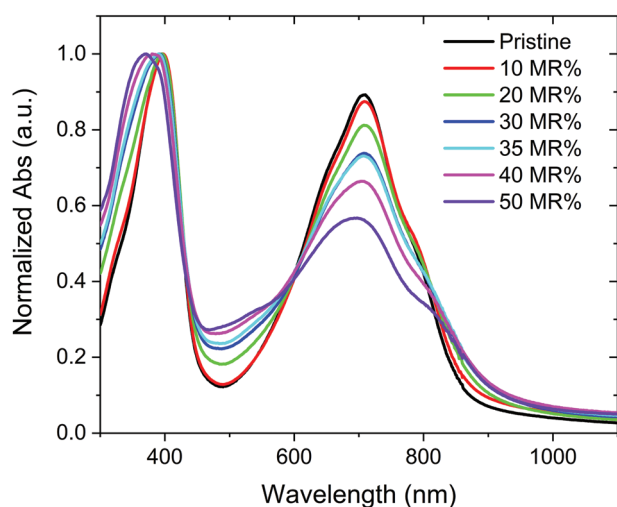


Figure 3. UV-vis-NIR normalized absorption spectra of P(NDI2OD-T2) thin films as a function of IStBI concentration (MR%) for samples annealed at 180 °C for 2 h and processed from toluene solution.

scopy.^[53,54] The intensity of the polaron-related bands follows an increasing trend as a function of dopant concentration, therefore the sample containing 50 MR% of IStBI displays a higher concentration of charged polymer species, which can be linked to an enhanced carrier density. Moreover, the ICT band absorption wavelength does not seem to be affected by IStBI content, therefore the aggregation state seems to be preserved confirming the AFM results. The π - π^* band is also affected showing a subtle blueshift as the dopant concentration is increased. This effect is also associated with the formation of the radical species, which, as reported in literature, are characterized by an absorption peak at slightly higher energies compared to the one of the neutral polymer.^[53] Comparing these results with the spectra of samples prepared following the same protocol but with N-DMBI, as presented in Figure S8 in the Supporting Information, it can be observed that the above mentioned polaronic features are more evident in the case of IStBI doping at each molar concentration. This finding suggests in a qualitative way that the doping efficiency is higher when considering the novel derivative.

2.6. Electrical and Thermoelectric Characterization

Figure 4a reports the σ values of P(NDI2OD-T2) thin films doped with IStBI concentrations ranging from 0 to 50 MR%. Samples containing the two reference dopants, N-DMBI and N-DPBI, and prepared following the same processing conditions, were also fabricated and analyzed for comparison. The maximum σ values recorded for these reference derivatives are in line with those reported in the literature.^[32,33,44] Electrical conductivity as a function of the amount of added IStBI follows an increasing trend, reaching a maximum of $(1.14 \pm 0.13) \times 10^{-2} \text{ S cm}^{-1}$ at a concentration of 35 MR%, constituting an increase of almost five orders of magnitude with respect to $\sigma \approx 10^{-7} \text{ S cm}^{-1}$ characterizing pristine P(NDI2OD-T2).^[32] A further increase in dopant concentration however leads to a decrease of σ . As highlighted in **Figure 4b**, the maximum σ value achieved in the present work is the highest so far reported for solution-doped P(NDI2OD-T2) using benzimidazole

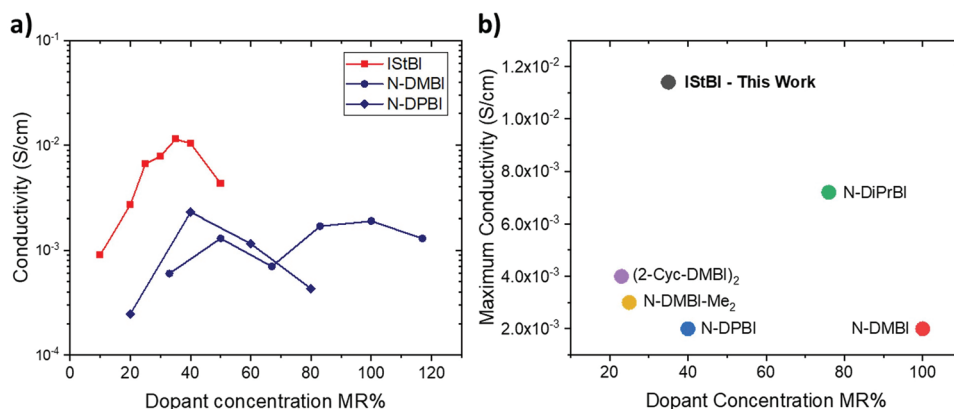


Figure 4. a) Room temperature electrical conductivity as a function of dopant concentration for toluene-cast P(NDI2OD-T2) thin films doped with benzimidazole derivatives: IStBI, N-DMBI, and N-DPBI. All the samples have been thermally annealed at 180 °C for 2 h. b) Comparison of the maximum electrical conductivity achieved for P(NDI2OD-T2) thin films depending on dopant concentration for different benzimidazole derivatives.^[26,32,33]

derivatives, showing an improvement of three to five times compared to the other compounds studied in the literature.^[20,26,32,33] Considering the observations made on the microstructural properties of the thin film, we can directly connect this value to the evidences of efficient dopant intercalation, which we can speculate to be responsible of better charge transfer efficiency between dopant and semiconductor.

As shown in Figure S9 in the Supporting Information, this enhancement of the conductivity was obtained performing a postdeposition thermal annealing step at 180 °C, which corresponds to the fusion point of the IStBI derivative measured in the DSC (Figure S2, Supporting Information). In agreement with the reports of Fabiano and co-workers on sequentially doped poly(benzimidazobenzophenanthroline) with N-DMBI, we assign this behavior to an improved dopant diffusivity reached after its melting.^[13] Coherently with the just mentioned work, the drop observed at 200 °C can be assigned to IStBI degradation approaching the thermal stability limit previously evidenced by the TGA (Figure S1, Supporting Information). Interestingly, it was found that the thermal treatment is not essential to activate the doping process. Indeed, Figure S10 in the Supporting Information shows that samples which did not undergo any annealing step already possess a σ in the range of 10^{-3} S cm⁻¹ just upon solvent evaporation. It must be noted that σ for the nonannealed samples does not show a strong dependence on IStBI content; moreover, these values are almost comparable to those obtained with the other benzimidazoles, like N-DMBI, after performing the thermal treatment.

We completed the characterization of the thermoelectric properties of the doped films by measuring the in-plane Seebeck coefficient at room temperature using a custom-built setup.^[55] All the investigated samples are characterized by a negative S value as expected for n-type doped materials (Figure 5). The S values, for the dopant concentration range between 20 and 50 MR%, decrease from -127.8 ± 2.6 to -9.3 ± 0.8 μ V K⁻¹. The observed trend as a function of increasing dopant concentration further confirms, as evidenced through UV-vis spectroscopy, that the addition of IStBI is effective in increasing the number of carriers in the semiconductor blend. Then, a decrease in the charge mobility must be accounted for the measured drop in σ at high doping concentrations. This finding can be assigned

either to a higher degree of structural disorder or to Coulomb trapping effects related to the presence of ionized dopant counterions in the polymeric matrix.^[56–58] The highest power factor PF is achieved at a concentration of 20 MR% and estimated to be $(4.2 \pm 0.3) \times 10^{-3}$ μ W m⁻¹ K⁻². It has to be noted that the PF measured for the sample containing 35% MR of IStBI is very close to the maximum recorded value, which confirms the validity of the σ maximization approach, also considering that the final realization of working thermoelectric devices gains great benefit from an overall reduction in electrical resistance, since the conversion efficiency scales with the reciprocal of the total internal device resistance.^[59]

It is worth underlying that due to the intrinsic limitations of P(NDI2OD-T2) in achieving high conductivities, owing to strongly localized charge carriers,^[13] the obtained performances are not yet sufficient to apply this blend formulation to realize efficient OTEGs. Nevertheless, recently, OTEGs have been fabricated exploiting n-type materials characterized by a σ in the range of 10^{-1} S cm⁻¹, reaching power output densities of tens of

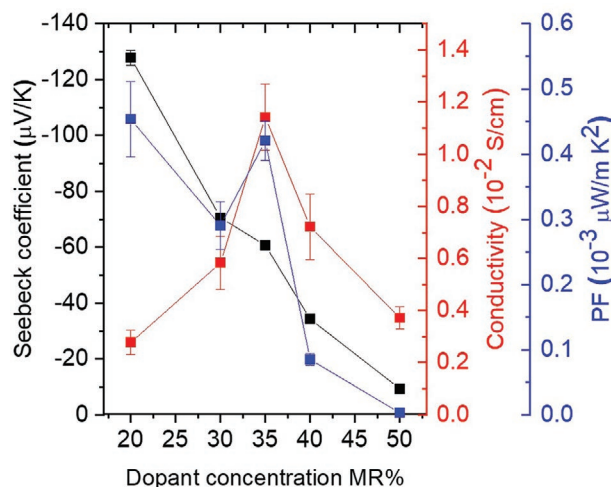


Figure 5. Thermoelectric parameters: Seebeck coefficient (black line), electrical conductivity (red line), and power factor (blue line) of doped P(NDI2OD-T2) samples at increasing IStBI concentration (MR%), collected at room temperature.

nW cm^{-2} . Therefore, it cannot be excluded that, by combining further improvements on the doping process with device architecture optimization, the use of P(NDI2OD-T2) would allow to reach thermoelectric properties relevant for applications.^[60]

3. Conclusion

We presented the use of an improved molecular dopant of the benzimidazoline derivatives family featuring the presence of an iminostilbene substituent. We assessed its doping effect in blends with the model electron transporting P(NDI2OD-T2), in comparison with well-known benzimidazoline derivatives. The new molecule features an improved planarity and a better miscibility in the target semiconducting polymer. The combination of such two features enhances the efficiency of the n-type doping performed with a solution-based approach. The achieved maximum σ of $(1.14 \pm 0.13) \times 10^{-2} \text{ S cm}^{-1}$ marks an increase of almost one order of magnitude with respect to the value obtained using the reference N-DMBI molecule. Since the performed functionalization does not cause a significant modification of the redox activity of the compound, as evidenced by electrochemical measurements, we can infer that stronger dopant-semiconductor solid-state interactions can be accounted for the electrical conductivity improvement. The absence of evident surface segregation further supports this claim. Indeed, despite a partial disruption of the long-range order occurring upon dopant loading, the morphological evidence arising from GIWAXS and AFM characterization is that the short-range interconnectivity is preserved, allowing efficient charge transport in the thin films. The increase in electrical conductivity comes at the expense of the Seebeck coefficient which is reduced when increasing the IStBI concentration. As a result of this trade-off, the maximum PF reached is $(4.2 \pm 0.3) \times 10^{-3} \mu\text{W m}^{-1} \text{ K}^{-2}$. Even if the improvement in terms of thermoelectric figure of merit that we report is numerically limited by the intrinsic characteristics of P(NDI2OD-T2), our investigation provides evidence that tailoring the benzimidazoline structure is an effective strategy to substantially modulate electrical conductivity in organic semiconductors thin films. We, therefore, deem as specific the results obtained for the doping of P(NDI2OD-T2), but as general the possibility to act on molecular interactions while leaving unaltered the electronic properties of the dopant. Indeed, further exploration of these chemical design concepts and the combination with better performing n-type materials can play a significant role toward the realization of technologically relevant applications. Bridging the gap with p-type materials is indeed crucial to improve the performances of OTEGs moving from the current few tens of nW with a footprint of a few cm^2 to the fabrication of devices characterized by a power of a few μW required for the operation of several IoT devices.

4. Experimental Section

Substrates Preparation for Conductivity Measurements: Corning glass (low alkali, 1737F) slides were precisely cut into $15 \text{ mm} \times 15 \text{ mm}$ pieces. Metallic contacts were patterned on the substrates through

a shadow mask by thermal evaporation (MB-ProVap-3) depositing a 3 nm Cr adhesion layer and a thick 50 nm Au layer. Each electrode is $3 \text{ mm} \times 15 \text{ mm}$ and the interelectrode distance is 5 mm.

Thermogravimetric Analysis: TGA measurements were performed with a TGA/DSC 1 STARe System from Mettler Toledo, using alumina crucibles. The analysis was performed with the following TGA method: heating from 35 to 400°C with a $10^\circ\text{C min}^{-1}$ rate, under 50 mL min^{-1} N_2 flow.

Differential Scanning Calorimetry: DSC measurements were performed with a DSC 1 STARe System from Mettler Toledo, in aluminum crucibles. Calibration was performed with Indium standard and the measurements were conducted under N_2 flow (80 mL min^{-1}). Further details are available in the Supporting Information.

Electrochemical Measurements: CV and DPV were performed in a three-electrode electrochemical cell equipped with a glassy carbon pin working electrode (Amel Electrochemistry, diameter = 3 mm), a platinum wire counter electrode, and an Ag/AgCl reference electrode. The redox couple Fc^+/Fc was used as an internal reference for all the measured potentials. The electrolyte solution was prepared adding to anhydrous acetonitrile (99.8% Alfa Aesar) the dopant and tetrabutylammonium perchlorate (99% Thermo Scientific) at a concentration of 2.0 and 0.1 mM respectively. The electrochemical cell was handled in an Ar-filled glovebox (MBraun) and connected to a potentiostat (Autolab PGSTAT302N) for the recording. CV was performed with a scan-rate of 50 mV s^{-1} , while the DPV with 2 mV s^{-1} steps and a modulation amplitude of 25 mV. A scan-rate dependent correction is applied to all the reduction potentials recorded by CV.

Thin Films Deposition: A stock solution of P(NDI2OD-T2) (Polyera ActivInk N2200 $M_n = 37.4 \text{ kDa}$, with a polydispersity index of 2.1) in toluene (Sigma-Aldrich) was prepared with a concentration of 10 g L^{-1} , to ensure complete dissolution it was kept stirring at 60°C overnight. Using the same solvent, solutions of IStBI were prepared at a concentration of 5 g L^{-1} . Only fresh-made (<2 h) dopant solutions were used to exclude possible degradation effects, as detailed in Figure S11 in the Supporting Information.^[22] To perform solution doping, aliquots of dopant and polymer stock solutions were mixed at corresponding amounts to reach the selected doping concentration. The dopant concentration is expressed in MR%, which is calculated as the ratio between the number of dopant moles over that of polymer repeat units, to allow a better comparison with data available in the literature. Finally, toluene was added to adjust all the aliquots to the same polymer concentration. The glass substrates (both patterned and non-) were cleaned sequentially in deionized water, acetone and 2-propanol (Sigma-Aldrich) submerged in an ultrasonic bath for 10 min each. Following, the substrates were exposed to a O_2 plasma (Femto Diener electronic) at 100 W for 10 min. The thin films were cast via spin-coating technique inside a N_2 -filled glovebox (MBraun), the deposition parameters were 1000 rpm for 60 s followed by 3000 rpm for 10 s. The samples were then thermally annealed on a hotplate for 2 h and at a temperature comprised in the $120\text{--}200^\circ\text{C}$ range. A thickness in the range of $65 \pm 5 \text{ nm}$ for all the films was determined using a mechanical profilometer (Alpha-step IQ, KLA Tencor). The same protocol was applied with samples containing N-DMBI and N-DPBI.

GIWAXS Measurements: GIWAXS measurements were performed at the small angle X-ray scattering/wide angle X-ray scattering (SAXS/WAXS) beamline at the Australian Synchrotron.^[61] 2D scattering patterns were recorded using a Pilatus 2 M detector, with the sample-to-detector distance calibrated using a silver behenate reference standard. The sample and detector were enclosed in a vacuum chamber to suppress air scatter. Scattering patterns were measured as a function of angle of incidence, with data shown acquired with an angle of incidence near the critical angle that maximized scattering intensity from the sample. Further detailed introduction can be found in previous publications.^[62]

AFM Imaging: AFM characterization was performed with an Agilent 5500 atomic force microscope operating in acoustic mode. Surface topography images were processed using Gwyddion image analysis software.

UV-vis-NIR Spectroscopy: The UV-vis-NIR absorptions spectra of the thin film samples were acquired in air using a double beam Perkin Elmer 11050 spectrophotometer in the $300\text{--}1100 \text{ nm}$ range.

Electrical Conductivity Measurements: The I - V characteristics were collected in the current saturation regime employing a two-point contact configuration by means of a probe-station (Wentworth Laboratories) connected to a semiconductor device parameter analyzer (Agilent B1500A). Measurements were performed at room temperature (RT) in a N_2 -filled glovebox. Forward and backward scans were performed to exclude the presence of hysteresis. The electrical conductivity values were subsequently calculated, considering the geometrical parameters, from the resistance values extrapolated from the I - V curves.

Seebeck Coefficient Measurements: The in-plane Seebeck coefficient measurements were performed using a custom setup built for thin films characterization and described in detail in the work of Beretta et al.^[55] The measurements were conducted at RT and under vacuum conditions (10^{-4} mbar) to reduce convection phenomena and to avoid samples oxidation. Due to the instrumentation limitations only samples with an electrical resistance below 10 M Ω could be measured.

Supporting Information

Supporting Information is available from the Wiley Online Library or from the author.

Acknowledgements

GIWAXS experiments were performed on the SAXS/WAXS beamline43 at the Australian Synchrotron, part of Australian Nuclear Science and Technology Organization (ANSTO). L.B., S.M., and F.P. gratefully acknowledge the financial contribution from Ministry of Education, University and Research (MIUR) under Grant "Dipartimenti di Eccellenza 2017 Project—Materials for Energy" and Grant PRIN2017 BOOSTER (2017YXX8AZ). M.C. acknowledges support under the European Union's Horizon 2020 research and innovation programme "GREENELIT", Grant Agreement No. 951747. P.R. wishes to thank Dr. Alessandro Luzzio for the fruitful discussion on paper preparation. This work falls within the Sustainability Activity of Istituto Italiano di Tecnologia.

Conflict of Interest

The authors declare no conflict of interest.

Data Availability Statement

The data that support the findings of this study are available from the corresponding author upon reasonable request.

Keywords

benzimidazoline derivatives, molecular doping, organic thermoelectrics, P(NDI2OD-T2)

Received: November 30, 2022
Revised: February 9, 2023
Published online: April 2, 2023

- [1] A. D. Scaccabarozzi, A. Basu, F. Aniés, J. Liu, O. Zapata-Arteaga, R. Warren, Y. Firdaus, M. I. Nugraha, Y. Lin, M. Campoy-Quiles, *Chem. Rev.* **2021**, 122, 4420.
- [2] S. Reineke, F. Lindner, G. Schwartz, N. Seidler, K. Walzer, B. Lüssem, K. Leo, *Nature* **2009**, 459, 234.

- [3] Y. Lin, Y. Firdaus, M. I. Nugraha, F. Liu, S. Karuthedath, A. Emwas, W. Zhang, A. Seikhan, M. Neophytou, H. Faber, *Adv. Sci.* **2020**, 7, 1903419.
- [4] D. Khodagholy, J. Rivnay, M. Sessolo, M. Gurfinkel, P. Leleux, L. H. Jimison, E. Stavrinidou, T. Herve, S. Sanaur, R. M. Owens, *Nat. Commun.* **2013**, 4, 2133.
- [5] A. F. Paterson, Y. Lin, A. D. Mottram, Z. Fei, M. R. Niazi, A. R. Kirmani, A. Amassian, O. Solomeshch, N. Tessler, M. Heeney, *Adv. Electron. Mater.* **2018**, 4, 1700464.
- [6] D. Beretta, N. Neophytou, J. M. Hodges, M. G. Kanatzidis, D. Narducci, M. Martin-Gonzalez, M. Beekman, B. Balke, G. Cerretti, W. Tremel, *Mater. Sci. Eng., R* **2019**, 138, 100501.
- [7] N. Pataki, P. Rossi, M. Caironi, *Appl. Phys. Lett.* **2022**, 121, 230501.
- [8] O. Zapata-Arteaga, A. Perevedentsev, S. Marina, J. Martin, J. S. Reparaz, M. Campoy-Quiles, *ACS Energy Lett.* **2020**, 5, 2972.
- [9] K. Gordiz, A. K. Menon, S. K. Yee, *J. Appl. Phys.* **2017**, 122, 124507.
- [10] O. Bubnova, Z. U. Khan, A. Malti, S. Braun, M. Fahlman, M. Berggren, X. Crispin, *Nat. Mater.* **2011**, 10, 429.
- [11] G.-H. Kim, L. Shao, K. Zhang, K. P. Pipe, *Nat. Mater.* **2013**, 12, 719.
- [12] S. Griggs, A. Marks, H. Bristow, I. McCulloch, *J. Mater. Chem. C* **2021**, 9, 8099.
- [13] S. Wang, T.-P. Ruoko, G. Wang, S. Riera-Galindo, S. Hultmark, Y. Puttisong, F. Moro, H. Yan, W. M. Chen, M. Berggren, *ACS Appl. Mater. Interfaces* **2020**, 12, 53003.
- [14] A. Barbot, B. Lucas, C. di Bin, B. Ratier, *Org. Electron.* **2014**, 15, 858.
- [15] S. Guo, S. B. Kim, S. K. Mohapatra, Y. Qi, T. Sajoto, A. Kahn, S. R. Marder, S. Barlow, *Adv. Mater.* **2012**, 24, 699.
- [16] P.-C. Kao, J.-H. Lin, J.-Y. Wang, C.-H. Yang, S.-H. Chen, *J. Appl. Phys.* **2011**, 109, 094505.
- [17] Y. Lu, J.-Y. Wang, J. Pei, *Acc. Chem. Res.* **2021**, 54, 2871.
- [18] P. Wei, J. H. Oh, G. Dong, Z. Bao, *J. Am. Chem. Soc.* **2010**, 132, 8852.
- [19] H. Wang, P. Wei, Y. Li, J. Han, H. R. Lee, B. D. Naab, N. Liu, C. Wang, E. Adjianto, B. C.-K. Tee, *Proc. Natl. Acad. Sci. U.S.A.* **2014**, 111, 4776.
- [20] R. A. Schlitz, F. G. Brunetti, A. M. Glaudell, P. L. Miller, M. A. Brady, C. J. Takacs, C. J. Hawker, M. L. Chabinyc, *Adv. Mater.* **2014**, 26, 2825.
- [21] O. Bardagot, C. Aumaitre, A. Monmagnon, J. Pécaut, P.-A. Bayle, R. Demadrille, *Appl. Phys. Lett.* **2021**, 118, 203904.
- [22] F. Pallini, S. Mattiello, M. Cassinelli, P. Rossi, S. Mecca, W. L. Tan, M. Sassi, G. Lanzani, C. R. McNeill, M. Caironi, L. Beverina, *ACS Appl. Energy Mater.* **2022**, 5, 2421.
- [23] H. Guo, C.-Y. Yang, X. Zhang, A. Motta, K. Feng, Y. Xia, Y. Shi, Z. Wu, K. Yang, J. Chen, Q. Liao, Y. Tang, H. Sun, H. Y. Woo, S. Fabiano, A. Facchetti, X. Guo, *Nature* **2021**, 599, 67.
- [24] J. Liu, L. Qiu, G. Portale, M. Koopmans, G. ten Brink, J. C. Hummelen, L. J. A. Koster, *Adv. Mater.* **2017**, 29, 1701641.
- [25] Y. Zeng, W. Zheng, Y. Guo, G. Han, Y. Yi, *J. Mater. Chem. A* **2020**, 8, 8323.
- [26] B. D. Naab, S. Zhang, K. Vandewal, A. Salleo, S. Barlow, S. R. Marder, Z. Bao, *Adv. Mater.* **2014**, 26, 4268.
- [27] A. Marks, X. Chen, R. Wu, R. B. Rashid, W. Jin, B. D. Paulsen, M. Moser, X. Ji, S. Griggs, D. Meli, X. Wu, H. Bristow, J. Strzalka, N. Gasparini, G. Costantini, S. Fabiano, I. McCulloch, *J. Am. Chem. Soc.* **2022**, 144, 4642.
- [28] K. Shi, F. Zhang, C.-A. Di, T.-W. Yan, Y. Zou, X. Zhou, D. Zhu, J.-Y. Wang, J. Pei, *J. Am. Chem. Soc.* **2015**, 137, 6979.
- [29] J. Han, H. Fan, Q. Zhang, Q. Hu, T. P. Russell, H. E. Katz, *Adv. Funct. Mater.* **2021**, 31, 2005901.
- [30] C.-Y. Yang, M.-A. Stoeckel, T.-P. Ruoko, H.-Y. Wu, X. Liu, N. B. Kolhe, Z. Wu, Y. Puttisong, C. Musumeci, M. Massetti, H. Sun, X. K. D. Tu, W. M. Chen, H. Y. Woo, M. Fahlman, S. A. Jenekhe, M. Berggren, S. Fabiano, *Nat. Commun.* **2021**, 12, 2354.

- [31] H. Tang, Y. Liang, C. Liu, Z. Hu, Y. Deng, H. Guo, Z. Yu, A. Song, H. Zhao, D. Zhao, Y. Zhang, X. Guo, J. Pei, Y. Ma, Y. Cao, F. Huang, *Nature* **2022**, 611, 271.
- [32] B. Saglio, M. Mura, M. Massetti, F. Scuratti, D. Beretta, X. Jiao, C. R. McNeill, M. Sommer, A. Famulari, G. Lanzani, *J. Mater. Chem. A* **2018**, 6, 15294.
- [33] S. Riera-Galindo, A. Orbelli Biroli, A. Forni, Y. Puttisong, F. Tessore, M. Pizzotti, E. Pavlopoulou, E. Solano, S. Wang, G. Wang, T.-P. Ruoko, W. M. Chen, M. Kemerink, M. Berggren, G. di Carlo, S. Fabiano, *ACS Appl. Mater. Interfaces* **2019**, 11, 37981.
- [34] L. Qiu, J. Liu, R. Alessandri, X. Qiu, M. Koopmans, R. W. A. Havenith, S. J. Marrink, R. C. Chiechi, L. J. A. Koster, J. C. Hummelen, *J. Mater. Chem. A* **2017**, 5, 21234.
- [35] S. Wang, H. Sun, U. Ail, M. Vagin, P. O. Å. Persson, J. W. Andreasen, W. Thiel, M. Berggren, X. Crispin, D. Fazzi, *Adv. Mater.* **2016**, 28, 10764.
- [36] S. Bonacci, G. Iriti, S. Mancuso, P. Novelli, R. Paonessa, S. Tallarico, M. Nardi, *Catalysts* **2020**, 10, 845.
- [37] S. Mattiello, G. Lucarelli, A. Calascibetta, L. Polastri, E. Ghiglietti, S. K. Podapangi, T. M. Brown, M. Sassi, L. Beverina, *ACS Sustainable Chem. Eng.* **2022**, 10, 4750.
- [38] M. Marinescu, L. O. Cintează, G. I. Marton, M.-C. Chifriuc, M. Popa, I. Stănculescu, C.-M. Zălaru, C.-E. Stavarache, *BMC Chem.* **2020**, 14, 45.
- [39] X.-Q. Zhu, M.-T. Zhang, A. Yu, C.-H. Wang, J.-P. Cheng, *J. Am. Chem. Soc.* **2008**, 130, 2501.
- [40] H. Yan, Z. Chen, Y. Zheng, C. Newman, J. R. Quinn, F. Dötz, M. Kastler, A. Facchetti, *Nature* **2009**, 457, 679.
- [41] J. Rivnay, M. F. Toney, Y. Zheng, I. V. Kauvar, Z. Chen, V. Wagner, A. Facchetti, A. Salleo, *Adv. Mater.* **2010**, 22, 4359.
- [42] J. Rivnay, R. Steyrlleuthner, L. H. Jimison, A. Casadei, Z. Chen, M. F. Toney, A. Facchetti, D. Neher, A. Salleo, *Macromolecules* **2011**, 44, 5246.
- [43] M. Kang, J. Yeo, W. Park, N. Kim, D. Lim, H. Hwang, K. Baeg, Y. Noh, D. Kim, *Adv. Funct. Mater.* **2016**, 26, 8527.
- [44] D. Nava, Y. Shin, M. Massetti, X. Jiao, T. Biskup, M. S. Jagadeesh, A. Calloni, L. Duò, G. Lanzani, C. R. McNeill, *ACS Appl. Energy Mater.* **2018**, 1, 4626.
- [45] S. Wang, S. Fabiano, S. Himmelberger, S. Puzinas, X. Crispin, A. Salleo, M. Berggren, *Proc. Natl. Acad. Sci. U.S.A.* **2015**, 112, 10599.
- [46] R. Noriega, J. Rivnay, K. Vandewal, F. P. v Koch, N. Stingelin, P. Smith, M. F. Toney, A. Salleo, *Nat. Mater.* **2013**, 12, 1038.
- [47] D. Kiefer, A. Giovannitti, H. Sun, T. Biskup, A. Hofmann, M. Koopmans, C. Cendra, S. Weber, L. J. Anton Koster, E. Olsson, J. Rivnay, S. Fabiano, I. McCulloch, C. Müller, *ACS Energy Lett.* **2018**, 3, 278.
- [48] A. Luzio, L. Criante, V. D'Innocenzo, M. Caironi, *Sci. Rep.* **2013**, 3, 3425.
- [49] Y. Shin, M. Massetti, H. Komber, T. Biskup, D. Nava, G. Lanzani, M. Caironi, M. Sommer, *Adv. Electron. Mater.* **2018**, 4, 1700581.
- [50] L. Lei, W. Wang, C. Wang, H. Fan, A. K. Yadav, N. Hu, Q. Zhong, P. Müller-Buschbaum, *J. Mater. Chem. A* **2020**, 8, 23812.
- [51] N. Hu, W. Wang, L. Lei, H. Fan, Y. Tan, H. Yuan, Z. Mao, P. Müller-Buschbaum, Q. Zhong, *Green Chem.* **2021**, 23, 8969.
- [52] R. Steyrlleuthner, M. Schubert, I. Howard, B. Klaumünzer, K. Schilling, Z. Chen, P. Saalfrank, F. Laquai, A. Facchetti, D. Neher, *J. Am. Chem. Soc.* **2012**, 134, 18303.
- [53] D. Trefz, A. Ruff, R. Tkachov, M. Wieland, M. Goll, A. Kiri, S. Ludwigs, *J. Phys. Chem. C* **2015**, 119, 22760.
- [54] M. Caironi, M. Bird, D. Fazzi, Z. Chen, R. di Pietro, C. Newman, A. Facchetti, H. Sirringhaus, *Adv. Funct. Mater.* **2011**, 21, 3371.
- [55] D. Beretta, P. Bruno, G. Lanzani, M. Caironi, *Rev. Sci. Instrum.* **2015**, 86, 075104.
- [56] J. Liu, Y. Shi, J. Dong, M. I. Nugraha, X. Qiu, M. Su, R. C. Chiechi, D. Baran, G. Portale, X. Guo, L. J. A. Koster, *ACS Energy Lett.* **2019**, 4, 1556.
- [57] G. Zuo, H. Abdalla, M. Kemerink, *Phys. Rev. B* **2016**, 93, 235203.
- [58] S. Fratini, M. Nikolka, A. Salleo, G. Schweicher, H. Sirringhaus, *Nat. Mater.* **2020**, 19, 491.
- [59] D. Beretta, M. Massetti, G. Lanzani, M. Caironi, *Rev. Sci. Instrum.* **2017**, 88, 015103.
- [60] M. Massetti, S. Bonfadini, D. Nava, M. Butti, L. Criante, G. Lanzani, L. Qiu, J. C. Hummelen, J. Liu, L. J. A. Koster, *Nano Energy* **2020**, 75, 104983.
- [61] N. M. Kirby, S. T. Mudie, A. M. Hawley, D. J. Cookson, H. D. T. Mertens, N. Cowieson, V. Samardzic-Boban, *J. Appl. Crystallogr.* **2013**, 46, 1670.
- [62] E. Gann, M. Caironi, Y.-Y. Noh, Y.-H. Kim, C. R. McNeill, *Macromolecules* **2018**, 51, 2979.